Supporting information for

Deep versus shallow emplacement of sills and dykes: new insight from thermo-visco-elastic modelling

Harro Schmeling, Gernold Zulauf

Institute of Geosciences, Goethe University Frankfurt, Germany (H.S. retired)

Submitted to	Tectonophysics
Submission date	Jan., 18, 2024
Revised	April 2024
Accepted	May, 29, 2024

Content of this file

1. Text S1 to S6

2. Figures S1 to S4

Introduction

This file contains detailed descriptions of the theory used to derive the stress field of a planar inclusion undergoing contraction (S1), of the numerical scheme used to solve the visco-elastic equation (S2), of the formulation of the effective elasticity, rock rheology and aspects on the fluid pressure (S3). In S4, the stress evolution of Case 2 is shown and discussed. In S5 a detailed discussion and Figure on the Deborah number is presented. The text S6 discusses the limitations of the models. All variables used here are defined in Table 1 in the main text.

Text S1

Elastic stress determination of a planar inclusion undergoing volume change

In this supplement, we determine elastic stresses and strains of an infinite planar elastic inclusion embedded in an infinite elastic medium using the theory of Eshelby (1957). Eshelby's approach is illustrated in Fig. S1. At $t = 0$ the infinite elastic medium containing an ellipsoidal elastic inclusion with half axes $a = b \gg c$ is assumed being stress-free (Fig. S1 a). In the first step the inclusion is cut out from the host material and undergoes a homogeneous stress-free (unconstrained) strain e_{ij}^T, in our case a change in volume due to a phase change or thermal contraction (Fig. S1 b)

$$e_{ij}^T = e\,\delta_{ij} \tag{1}$$

with $e = \frac{1}{3}\frac{\Delta V}{V}$ as isotropic strain describing the relative volume change $\frac{\Delta V}{V}$ and δ_{ij} as Kronecker symbol (= 1 if $i = j$, else = 0). In the next step, surface tractions t_{ij}^T are applied to the inclusion to restore the original shape of the inclusion (Fig. S1 c). The inclusion is welded back to the matrix, which is still stress-free. In the next step, the tractions are relaxed by applying compensating tractions $-t_{ij}^T$ to the interface between matrix and inclusion assuming a homogeneous infinite medium (Fig. S1 d). Now force equilibrium at the interface is restored, the inclusion is constrained and undergoes a further strain e_{ij}^C (Fig. S1 d). In the general case of a finite inclusion, the matrix is stressed and strained, for an infinite planar inclusion not (see below). Eshelby (1957) derived the general relation between e_{ij}^T and the e_{ij}^C within the inclusion and showed that the constrained strain is homogeneous within an ellipsoidal inclusion

$$e_{ij}^C = S_{ijmn} e_{mn}^T \tag{2}$$

Here the summation convention is assumed. For the special case of an oblate inclusion lying within the yz-plane Eshelby's solution has the limits

$$S_{yyyy}, S_{yyxx}, S_{zzzz}, S_{zzxx} \sim \frac{c}{a} \to 0 \tag{3}$$

$$S_{xxxx} = 1 \tag{4}$$

$$S_{xxyy} = S_{xxzz} = \frac{\nu}{1-\nu} \tag{5}$$

From these relations we can determine the strains of a planar inclusion in the $yz-$ plane. From eq. (3) it follows with (2) that the constrained strain in inclusion-parallel direction, e_{yy}^C, e_{zz}^C , is proportional to $\frac{c}{a} \to 0$, i.e. for an infinite planar inclusion we have

$$e_{yy}^C = e_{zz}^C = 0 \tag{6}$$

Due to continuity across the interface, the same applies to the outside of the inclusion, i.e. the wall rock does not deform in y- and z - direction, i.e. it is stress- and strain-free in inclusion-parallel direction. This means that the cooling or solidification of an infinite inclusion is a uniaxial strain problem. In inclusion-orthogonal direction (x) the constrained strain is (using eq. (1), (2), (4), (5))

$$e_{xx}^C = S_{xxxx} e_{xx}^T + S_{xxyy} e_{yy}^T + S_{xxzz} e_{zz}^T = \frac{1+\nu}{1-\nu}\, e \tag{7}$$

With these constrained strains the stresses within the planar inclusion (i.e. dyke, sill, or any infinitesimal layer in the $yz-$ plane undergoing thermal contraction or expansion) can be calculated by adding a change of strain δe_{xx} to the stress-free strain e_{xx}^T and write for the constrained strain $e_{xx}^C = e_{xx}^T + \delta e_{xx} = e + \delta e_{xx} = \frac{1+\nu}{1-\nu} e$. Similar changes of strain δe_{yy} and δe_{zz} taken in the other directions. All these strains are

$$\delta e_{xx} = \frac{1+\nu}{1-\nu} e - e, \;\; \delta e_{yy} = -e, \;\; \delta e_{zz} = -e \tag{8}$$

Inserting these strains into Hooke's law one arrives at stresses inside the planar inclusion

$$\sigma_{\parallel} \equiv \sigma_{yy} = \sigma_{zz} = -\frac{E}{1-\nu} e \tag{9}$$

$$\sigma_{\perp} \equiv \sigma_{xx} = 0 \tag{10}$$

where inclusion parallel and orthogonal directions are indicated by the subscripts $\parallel, \perp$, respectively. Equation (10) is consistent with the solution of the momentum equation,

$$\frac{\partial \sigma_{ij}}{\partial x_j} = 0 \tag{11}$$

which reduces for the 1D case in the principal stress system parallel to the x-, y- and z-axes to

$$\frac{\partial \sigma_{xx}}{\partial x} = 0 \tag{12}$$

Assuming a stress-free boundary condition at $x = \pm\infty$, integration along x results in eq. (10) at any x – position, i.e. inside and outside the intrusion.

Text S2

Numerical scheme of the visco-elastic formulation

In the main text an equation was derived describing the stress evolution due to visco-elastic contraction in 1D

$$0 = \frac{1-\nu}{E}\dot{\sigma}_{\parallel} + \frac{3\eta_b+4\eta_s}{18\eta_b\eta_s}\sigma_{\parallel} + \frac{1}{3}\alpha\dot{T} + \frac{\Delta\rho}{3\rho_0}\dot{\varphi} \tag{13}$$

As there does not exist an analytical solution of eq. (13), it is solved numerically. An implicit Finite Difference - scheme is used where k denotes the time step:

$$0 = \frac{1-\nu}{E}\frac{\sigma_{\parallel_{k+1}}-\sigma_{\parallel_k}}{\Delta t} + \frac{3\eta_b+4\eta_s}{18\eta_b\eta_s}\sigma_{\parallel_{k+1}} + \frac{1}{3}\alpha\dot{T}_k + \frac{\Delta\rho}{3\rho_0}\dot{\varphi}_k \tag{14}$$

This can be solved for the new stress

$$\sigma_{\parallel_{k+1}} = \left(\sigma_{\parallel_k} - \Delta t\frac{E}{1-\nu}\left(\frac{1}{3}\alpha\dot{T}_k + \frac{\Delta\rho}{3\rho_0}\dot{\varphi}_k\right)\right)\left(1 + \Delta t\frac{E}{1-\nu}\left(\frac{3\eta_b+4\eta_s}{18\eta_b\eta_s}\right)_k\right)^{-1} \tag{15}$$

The time derivatives of temperature and melt fraction are taken at the time steps k and $k+1$, so that we have

$$\sigma_{\parallel_{k+1}} = \left(\sigma_{\parallel_k} - \frac{E}{1-\nu}\left(\frac{1}{3}\alpha(T_{k+1}-T_k) + \frac{\Delta\rho}{3\rho_0}(\varphi_{k+1}-\varphi_k)\right)\right)\left(1 + \Delta t\frac{E}{1-\nu}\left(\frac{3\eta_b+4\eta_s}{18\eta_b\eta_s}\right)_k\right)^{-1} \tag{16}$$

It should be noted that in eq. (16) we use an implicit formulation for the stress, but for simplicity the effective, stress-dependent viscosities are taken at the old time-step k. This equation is solved in MATLAB for any x – position using $T(x,t)$ and $\varphi(x,t)$ from solutions in section 4.

Text S3

Effective elasticity, rheology and melt pressure

Effective elasticity

In the presence of melt the effective elastic moduli of rock are reduced (Schmeling, 1985), while the Poisson ratio increases up to 0.5. We use the self-consistent elastic composite formulation given in Schmeling (1985). While in that paper a distinction between high and low frequency effective moduli

has been made, it follows from Fig. 6 of that paper, that for the cooling intrusion problem here the "relaxed" moduli are appropriate, i.e. the melt pressure of differently oriented melt inclusions has rapidly equilibrated. The effective Young's modulus and Poisson ratio are calculated as a function of melt porosity (i.e. melt fraction) assuming an aspect ratio of 0.2 for ellipsoidal melt inclusions. This aspect ratio has been found to predict a similar rock weakening as found for melt typically distributed within tapered melt tubes along grain edges (Schmeling, 1985).

We use the self-consistent solutions for the low frequency (relaxed) and high frequency (unrelaxed) elastic moduli derived by Schmeling (1985) and fit them to parametric regression formulas. Here both, the unrelaxed and relaxed moduli are given although in this paper only the low frequency ("relaxed") moduli will be used. It should be noted that in this section (S3) the term relaxation is used only for fluid pressure equilibration between differently oriented melt inclusions, not for visco-elastic relaxation as in the rest of this paper.

The disaggregation melt fraction φ_{disr}, φ_{disu} for relaxed and unrelaxed moduli, respectively, depends on the aspect ratio of the ellipsoidal melt inclusions α_i and can be fitted by:

$$\varphi_{disr} = \frac{\varphi_{0r}\alpha_i}{\left(\frac{\varphi_{0r}}{d_r}+\alpha_i\right)^{c_r}} \tag{17}$$

$$\varphi_{disu} = \frac{\varphi_{0u}\alpha_i}{\left(\frac{\varphi_{0u}}{d_u}+\alpha_i\right)^{c_u}} \tag{18}$$

For the relaxed case, the disaggregation melt fraction is identical for any fluid compressibility per definition. The fitting parameters are φ_{0r} = 0.988, d_r = 1.817, c_r = 1.56.

For the unrelaxed case the disaggregation melt fraction weakly depends on the fluid bulk modulus. For a bulk modulus > $0.07 \cdot 10^{11}$ Pa good fitting parameters are φ_{0u} = 0.721, d_u = 4.472, c_u = 1.20. If we scale the melt fraction by the disaggregation melt fraction

$$\varphi' = \frac{\varphi}{\varphi_{disr,u}} \tag{19}$$

the dry bulk modulus of Schmeling (1985) can be fitted by

$$K_d = K_0(1-\varphi') + 4\,\Delta K_0\,\varphi'(1-\varphi') \tag{20}$$

where K_0 is the intrinsic rock bulk modulus and $\Delta K_0 = c_K K_0$ is the maximum deviation from a linearly decreasing modulus function. The parameter c_K can be fitted by

$$c_K = c_2 + (c_1 - c_2)(1-\alpha_i)^{c_3} \tag{21}$$

with c_1 = -0.198, c_2 = -0.07, and c_3 = 3.25. The fully saturated bulk modulus can be derived using the Gassman relation (Schmeling, 1985)

$$K_s = K_0 \frac{K_d+F}{K_0+F}, \qquad F = \frac{K_f(K_0-K_d)}{\varphi(K_0-K_f)} \tag{22}$$

The relaxed shear modulus is defined by assuming pressure equilibration between the pores of different orientation. It can be fitted to the self-consistent solution by

$$\mu_r = \mu_0(1-\varphi') + 4\,\Delta\mu_r\,\varphi'(1-\varphi') \tag{23}$$

where μ_0 is the intrinsic rock shear modulus and $\Delta\mu_r = c_r\mu_0$ is the maximum deviation from a linearly decreasing modulus function. The parameter c_r can be fitted by

$$c_r = c_2 + (c_1 - c_2)(1-\alpha_i)^{c_3} \tag{24}$$

with c_1 = 0.048, c_2 = 0.01, and c_3 = 3.36.

The unrelaxed shear modulus is defined by assuming that any fluid pressure differences within pores of different orientation have not equilibrated yet. It can be approximated by

$$\mu_u = \mu_0(1-\varphi') + 4\,\Delta\mu_u\,\varphi'(1-\varphi') \tag{25}$$

with $\Delta\mu_u = c_u\mu_0$ with the parameter c_u fitted by

$$c_u = c_1 + c_2\alpha_i\,exp(c_3\alpha_i) \tag{26}$$

with the parameters c_1 = -0.0625, c_2 = -0.673, and c_3 = -8.334. For empty pores, the unrelaxed and relaxed shear moduli are equal.

Using standard relations the Young's modulus and Poisson ratio needed in eq. 13 can directly be determined. They are shown in Fig. S2 for $\alpha_i = 0.2$ as used in this paper.

Viscous rheology

For the shear viscosity of the solid, a stress- and temperature - dependent viscosity is taken for both the intrusion and ambient rock:

$$\eta_{sol} = 3^{-\frac{1+n}{2}} A^{-1} {\tau_{II}}^{1-n} exp\left(\frac{E_a}{RT}\right) \tag{27}$$

where τ_{II} is the second invariant of the deviatoric stress tensor, n is the power law exponent, E_a is the activation energy, R is the Gas constant, and A is the pre-exponential constant in the experimentally derived power-law relating principal stress difference with axial strain rate. Values for A, E_a, and n are taken from Kirby and Kronenberg (1987) for diabase representing the intrusion (sill or dyke), and for Westerly granite representing the ambient rock (Table 1, main text). The 2nd invariant of the deviatoric stress can be expressed in terms of the intrusion parallel normal stress, $\sigma_{\parallel}$, and one gets

$$\eta_{sol} = \frac{2^{\frac{n-1}{2}}}{3} A^{-1} \left|\sigma_{\parallel}\right|^{1-n} exp\left(\frac{E_a}{RT}\right) \tag{28}$$

In the presence of melt, the effective viscosity of the rock drops further. Schmeling et al. (2012) derived the non-dimensional porosity dependent part of the shear and bulk viscosity assuming melt distributed within ellipsoidal inclusions and determined simple regression formulas,

$$\eta'_{\varphi} = \left(1 - \frac{\varphi}{c_1}\right)^{k_1}, \qquad \eta'_b = c_2 \frac{(c_1 - \varphi)^{k_2}}{\varphi} \qquad \text{for } \varphi \leq c_1 \tag{29}$$

while for $\varphi > c_1$ both viscosities are zero. The parameters c_1, k_1, c_2, and k_2 depend on the aspect ratio of the melt inclusions (here we assume 0.2), and can be found in Schmeling et al. (2012). Combining eq. (28) and (29), the final shear and bulk viscosities are given as

$$\eta_s = \eta_{sol}(T, \sigma) \cdot \eta'_{\varphi}(\varphi), \qquad \eta_b = \eta_{sol}(T, \sigma) \cdot \eta'_b(\varphi) \tag{30}$$

For spherical melt inclusions, the viscosity drops to zero at about 50% melt, for ellipsoidal melt inclusions with aspect ratio 0.2 or melt distributed within tapered melt tubes along grain edges, the viscosity drops to 0 at about 31 % melt, for 0.1 at about 19% melt. These melt fractions (φ) are identified with the rheological critical melt percentages (RCMP). In our model, we choose the aspect ratio 0.2, i.e. a RCMP of 31.3%.

In our modeling the temperature-stress-φ-dependent viscosities are calculated at each position and time step k, to be used for the equation (16) for the new stress at timestep $k + 1$. Once the RCMP is exceeded, both the viscosities and the stress $\sigma_{\parallel}$ drop to zero. In the unmolten regions, the shear viscosity is given by the rock viscosity (eq. 28), while the bulk viscosity is infinite.

Melt pressure

At finite melt fraction, the melt is assumed to be connected. Thus, lateral variations of pore pressure are assumed to equilibrate by porous flow. This equilibration takes place by pore pressure diffusion, which is controlled by pore pressure diffusivity

$$\kappa_p = \frac{k_{\varphi}}{\varphi \eta_f (\beta_f + \beta_{\varphi})} \tag{31}$$

where k_{φ} is the permeability, η_f the melt viscosity, β_f the melt compressibility and $\beta_{\varphi} = -\frac{1}{\varphi}\frac{\partial \varphi}{\partial P}$ the pore space compressibility, also called formation compressibility. To test the possibility of pore pressure diffusion, let us assume $k_{\varphi} = \frac{d^2}{100}\varphi^3$ with d as grain size (e.g. 1 mm), $\varphi = 0.01$ to 0.2, and η_f, β_f , β_{φ} as given in Table 1 in the main text. The formation compressibility is estimated based on the formulation by Schmeling and Marquart (2014). With resulting pore pressure diffusivities (Table 1, main text) and a characteristic length scale of the intrusion (e.g. 0.4 m for Case 1), we get pressure

diffusion times of 1 to 100 sec for the intrusion material and 300 to 10^5 s for the ambient rock. The freezing time from 100% to 0 % melt fraction in the intrusion lasts about $2 \cdot 10^5$ s (Fig 3, main text), thus the pressure equalizes during that period. The melting and freezing times in the ambient rock are about 10^6 to 10^7 s, so even in the ambient rock the fluid pressure equilibrates relatively rapidly. This also applies to Case 2, where both time scales are longer by a factor 25.

In the presence of melt, we distinguish between two cases:

1) In the case where at some position the melt fraction exceeds the RCMP, the melt can be regarded as drained and the melt pressure and the stress $\sigma_{\|}$ are zero. No underpressure will build up and volume changes are allowed to build up stress-free. Any volume change due to freezing or melting is accommodated by stress-free intrusion-orthogonal contraction, not by intrusion parallel stresses. The other effects on stress evolution such as visco-elastic relaxation or thermal stresses are still present in regions below the RCMP. This behavior is realized in our formulation by setting the term $\frac{\Delta\rho}{3\rho_0}\dot{\varphi}$ in eq. (13) to zero if φ is above the RCMP at any position within the intrusion or the ambient rock.

2) In the case that the melt fraction is below the RCMP everywhere, volume changes due to freezing or melting contribute to the stress change as a response to freezing or melting. As pressure diffusion is assumed to happen instantaneously, the term $\frac{\Delta\rho}{3\rho_0}\dot{\varphi}$ is averaged over the partially molten region.

Although the melt pressure is assumed to equilibrate rapidly in our approach, it is interesting to estimate the instantaneous, undrained melt pressure as this melt pressure may drive porous melt flow. In our visco-elastic Maxwell rheology formulation, the stresses in the elastic and viscous elements are equal. Thus we can estimate the undrained fluid pressure by using the Skempton coefficient B, which is defined in poro-elasticity as the ratio of the pore fluid pressure to the ambient pressure. B can be determined by using the intrinsic, dry, and saturated rock bulk moduli, K_0, K_d, K_s, respectively (Bagdassarov, 2022)

$$B = \frac{K_s - K_d}{K_0 - K_d} \cdot \frac{K_0}{K_s} \tag{32}$$

which can be calculated as a function of melt fraction using the equations given above (Supporting information S2).

Text S4

Visco-elastic stress evolution of shallow emplacement Case 2

Here a detailed discussion of the stress evolution of Case 2 is given. Fig. S3a shows the stress evolution of Case 2. Several differences to the hotter Case 1 are observed (c.f. Fig. 4, main text): Heating of the wall rock leads to stronger compressive stresses (blue band penetrating into the wall rock, Fig. S3a) followed by tensile stresses upon cooling after about 10^7 s to 10^8 s (green-yellowish region). As the amount of melting in the wall rock is very low (Fig. 3d, main text), the effect of ambient rock melting on the stress evolution is almost negligible; only a short freezing event at around 10^7 s generates some tensile stresses within a short distance to the dyke (narrow, short orange band in Fig. S3a). This is the only period, when the intrusion-parallel tensile stress in the wall rock is higher than the tensile stress in the sill/dyke. Intrusion-parallel tensile stresses in the sill/dyke occur later compared to Case 1. As the sill/dyke cools and continues to solidify, tensile stresses start to develop after $4 \cdot 10^6$ s (1 month) with a strong subsequent increase to 400 MPa at ca. 10 years (Fig. S3a). Subsequent to 10^7 s, the tensile stress in the sill/dyke is much larger compared to the tensile stress in the adjacent wall rock (Fig. S3a). The same holds for Case 1 (Fig. 4a). The low background temperatures lead to high viscosities (Fig. S3c) and associated long Maxwell times up to $2 \cdot 10^{13}$ s (0.7 Ma) (Fig. S3d) so that the stresses do not relax on the timescale shown. This will be confirmed below (Supporting information S5) when generalizing the results in terms of the Deborah number, which will be used to distinguish relaxed from unrelaxed regimes.

Text S5

Timescales, Deborah number

Here we explore the cooling Deborah number for various intrusion widths and rock viscosities (Fig. S4). In general, at small width De_{cool} strongly increases to values above 1. This means that stresses within the intrusion or wall rock are still unrelaxed for narrow intrusions during the cooling process. They relax at times much later than the intrusion cools completely. Stresses in wider intrusions relax faster than the intrusion cools, i.e. they are already relaxed during the cooling process.

The lower the rock viscosity, the smaller is De_{cool} (black to red curves in Fig. S4). This means that mechanically weak rocks are preferably associated with relaxed stresses already during their cooling process. When applying the viscosities and intrusion widths of our Case 1, the cooling Deborah numbers are high (>1) within the intrusion and the wall rock (Fig. S4, vertical lines). Thus, the stresses are unrelaxed on a time scale typically for cooling. In contrast, for Case 2 the Deborah number of the wall rock temporarily falls below 1, and the stresses relax on the cooling time scale. Only within the

intrusion, the viscosity is always high, so that a high Deborah number predicts unrelaxed stresses during the complete cooling time scale.

It is interesting to note that Case 2 has a 5 times wider intrusion layer, which would promote a lower Deborah number and a relaxed state, but this case is significantly cooler resulting in a more viscous rheology associated with a higher Deborah number and unrelaxed stresses. Obviously, these two effects are competitive, but in our particular example, the width-effect dominates for the wall rock in Case 2, leading to at least some relaxed stresses in the shallower wall rock of Case 2.

Text S6

Limitations of the models

The neglect of stresses due to the emplacement process has been discussed in section 5.1 of the main text (Brittle failure). Here we add that any ambient stresses will superimpose with the thermal stresses and non-linearly affect the power-law viscosity of the wall rock: If stresses add up, the viscosity will decrease as well as the Maxwell time. If the components of thermal and ambient stresses have different signs, the effective viscosity and Maxwell time might increase.

While we assumed an infinite dyke or sill, typical length to thickness ratios of mafic and felsic dykes or sills follow a logarithmic scaling law (e.g. Cruden et al. 2017) giving ratios between 10 and 1000 for a dyke or sill of the order of 1 m thickness. In a dyke or sill of finite length all stresses which are not associated with the 1D solution are expected to scale with the intrusion aspect ratio (Eshelby, 1957), i.e. a finite intrusion length would change the calculated stresses by 10% to 0.1% given the above-mentioned length to thickness ratios.

Dykes or sills are not perfectly planar. Turns of dykes during propagation and possible changes into sills occur over a finite distance if the stress field is heterogeneous or the driving pressure in the igneous sheet is very high (Dahm, 2000). Growth barriers are important in such cases (e.g. Kavanagh et al., 2006; Maccaferri et al., 2011; Gudmundsson, 2011). We speculate that the solidification of non-planar intrusions is expected to generate thermal stresses with deviations from our solutions of the order of intrusion thickness divided by the local curvature radius.

The assumption of constant thickness of the intrusion limits the results. Most of the dykes and sills in nature show striking variations in aperture (Gudmundsson, 1983), which in part could result from non-linear remote stress and internal pressure distributions, or from spatial variations in elastic stiffness (Townsend et al., 2017). On first order, 1D results for dykes of different thicknesses may be applicable to the same natural dyke with lateral thickness variations, while deviations are expected

to scale with the thickness of the dyke or sill to length scale (wavelength) of thickness variations. The influence of mechanical heterogeneity and anisotropy has not been addressed, although it may play a significant role during sill or dyke formation by creating stress barriers (Gudmundsson, 2002).

While we evaluated thermal and visco-elastic time-scales, the time-scale of the intrusion process may also play an important role. Propagation velocities of magma-filled fractures are expected to be of the order of 0.1 to 100 m/s (Dahm, 2000) and may be used to estimate typical emplacement times of the order 10^4 s to 10 s for a 1 km crack. Thus, the early stages of our models may still be concurrent with the emplacement process.

References

Bagdassarov, N., 2022. Fundamentals of Rock Physics, Cambridge University Press, Cambridge. doi: 10.1017/9781108380713

Cruden, A.R., McCaffrey, K.J.W., & Bunger, A.P., 2017. Geometric Scaling of Tabular Igneous Intrusions: Implications for Emplacement and Growth, In: Breitkreuz, C., Rocchi, S. (eds) Physical Geology of Shallow Magmatic Systems, Advances in Volcanology, Springer, Cham. https://doi.org/10.1007/11157_2017_1000

Dahm, T., 2000. Numerical simulations of the propagation path and the arrest of fluid-filled fractures in the Earth, Geophys. J. Int., 141, 623-638.

Eshelby, J. D., 1957. The determination of the elastic field of an ellipsoidal inclusion, and related problems, Proceedings of the royal society of London. Series A. Mathematical and physical sciences 241.1226: 376-396.

Gudmundsson, A., 1983. Form and dimensions of dykes in eastern Iceland, Tectonophysics, 95, 295–307.

Gudmundsson, A., 2002. Emplacement and arrest of sheets and dykes in central volcanoes, J. Volcanol. Geotherm. Res., 116, 279–298.

Gudmundsson, A., 2011. Deflection of dykes into sills at discontinuities and magma chamber formation, Tectonophysics, 500, 50–64.

Kavanagh, J.L., Menand, T., & Sparks, R.S.J., 2006. An experimental investigation of sill formation and propagation in layered elastic media, Earth Planet. Sc. Lett, 245, 799-813.

Kirby, S. H., & Kronenberg, A. K., 1987. Correction to “Rheology of the lithosphere: Selected topics”, Rev. Geophys. 25, 1680 – 1681.

Maccaferri, F., Bonafede, M., & Rivalta, E., 2011. A quantitative study of the mechanisms governing dike propagation, dike arrest and sill formation, J. Volcanol. Geotherm. Res., 208, 39-50.

Schmeling, H., 1985. Numerical models on the influence of partial melt on elastic, anelastic, and electric properties of rocks. Part I: elasticity and anelasticity, Phys. Earth Planet. Int., 41, 34-57.

Schmeling, H., Kruse, J.-P., & Richard, G., 2012. Effective shear and bulk viscosity of partially molten rock based on elastic moduli theory of a fluid filled poroelastic medium, Geophys. J. Int., 190, 1571 – 1578. doi: 10.1111/j.1365-246X.2012.05596.x

Schmeling, H., & Marquart, G., 2014. A scaling law for approximating porous hydrothermal convection by an equivalent thermal conductivity: theory and application to the cooling oceanic lithosphere, Geophys. J. Int., 197 (2), 645-664. doi:10.1093/gji/ggu022

Townsend, M. R., Pollard, D. D., & Smith, R. P., 2017. Mechanical models for dikes: a third school of thought, Tectonophysics, 703, 98-118

Figures S1 to S4

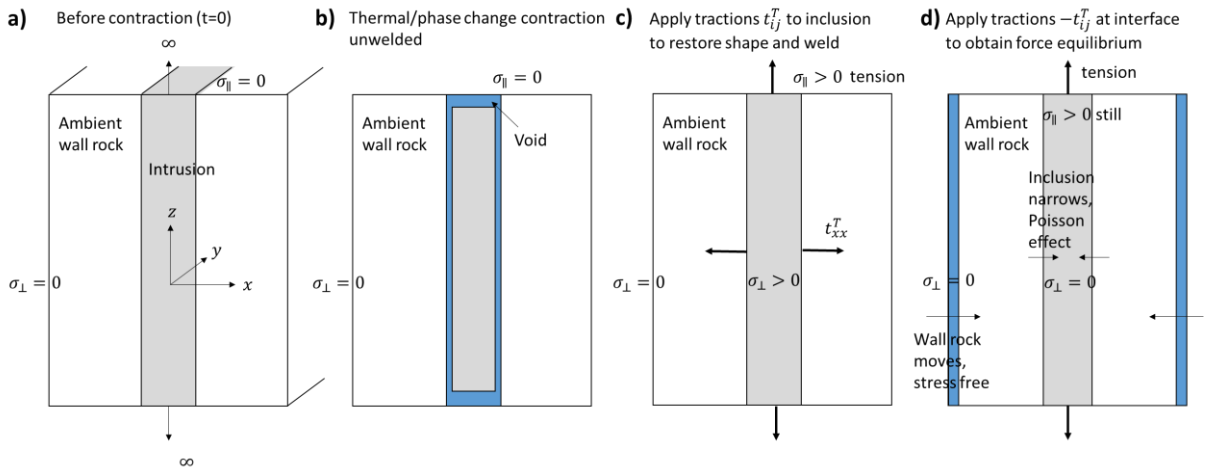

Figure S1: Illustration of steps needed for calculation of stresses of a shrinking elastic infinite inclusion after Eshelby (1957). See text.

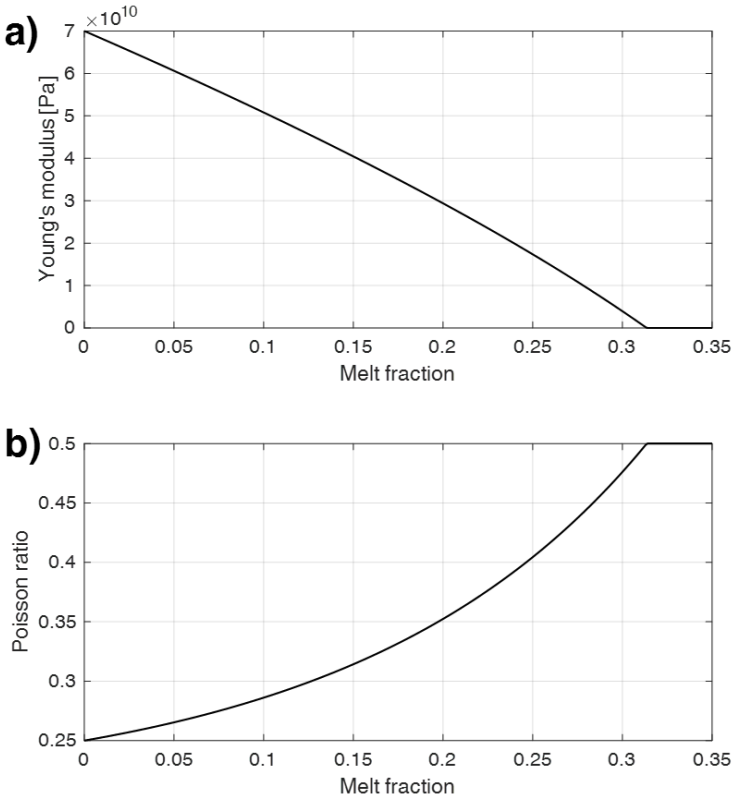

Figure S2: a) Effective Young's modulus and b) Poisson ratio as function of melt fraction resulting from the fitting formulas (17) to (26). These elastic properties are used in this paper.

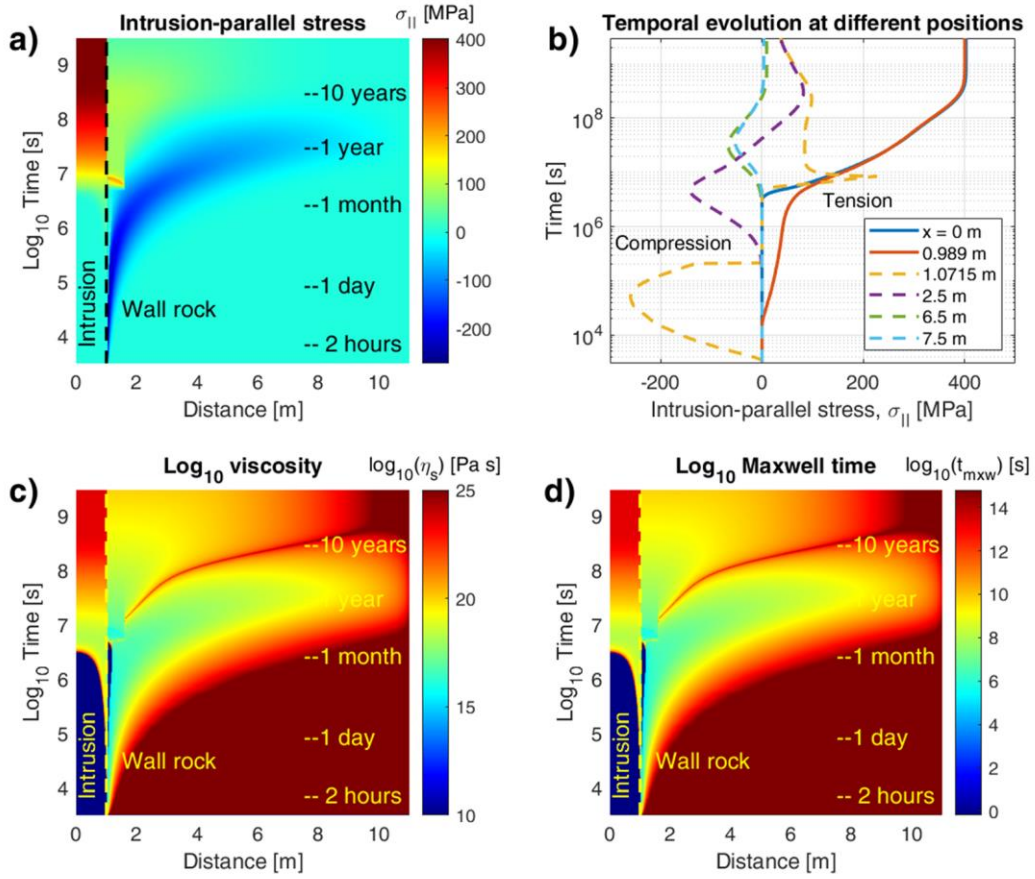

Figure S3: Case 2: Evolution of intrusion-parallel normal stress $\sigma_{\|}$(a and b), viscosity (c), and Maxwell time (d) of a planar intrusion and ambient wall rock due to cooling, heating, melting, solidification, and visco-elastic relaxation. The thermal and melt fraction evolution is the same as for the model shown in Fig. 4. In b) the solid curves represent stresses within the dyke, while the dashed curves show the stresses within the ambient rock at the indicated positions. The dyke-ambient rock contact is at x = 1 m (vertical dashed lines).

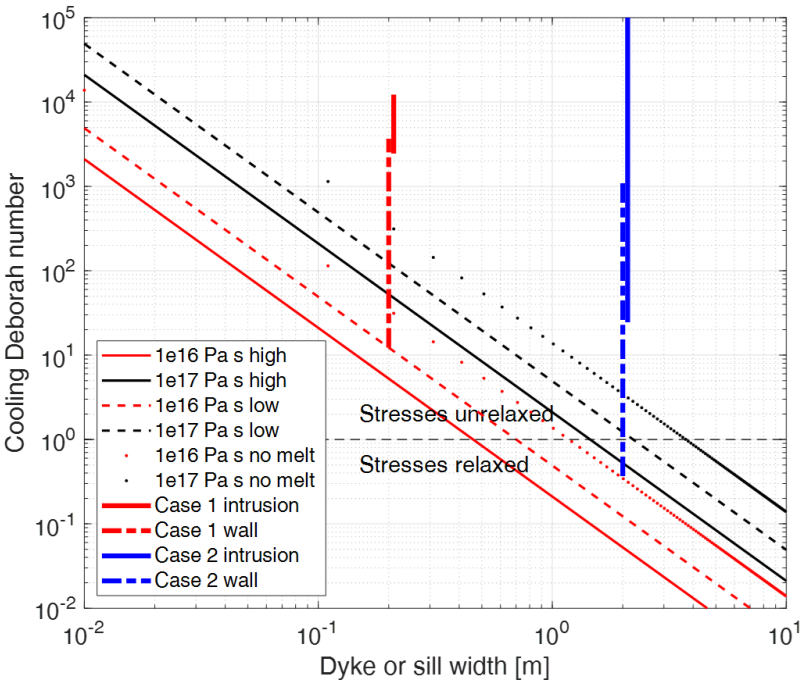

Figure S4: Cooling Deborah number versus intrusion width for different shear viscosities of the solid or partially molten rock. The bold thin lines use a shear to bulk viscosity ratio 1, which is expected for high melt fractions close to the RCMP. The dashed lines use and infinite bulk viscosity, typical for low melt fractions. The dotted lines use zero latent heat, infinite bulk viscosity and the shear viscosity of solid rock, i.e. no melt. The thin dashed line at $De_{cool} = 1$ separates the unrelaxed from the relaxed visco-elastic domains. The bold vertical lines approximate the cooling Deborah numbers of Case 1 and 2 for the intrusion and wall rock, respectively. The "intrusion" lines are offset by a small amount to better visualize the overlaps.